Desalination 586 (2024) 117857

Contents lists available at ScienceDirect

Desalination

journal homepage: www.elsevier.com/locate/desal

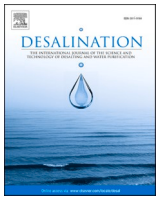

Desalination performance in versatile capacitive/battery deionization configurations using a cation intercalating electrode

Bethwel Kipchirchir Tarus [a,b,c], Zahid Ullah [a,b], Yusufu A.C. Jande [c,*], Karoli N. Njau [d], Jeehye Byun [a,b,**], Moon Son [a,b,**]

[a] Center for Water Cycle Research, Korea Institute of Science and Technology, 5 Hwarang-ro 14-gil, Seongbuk-gu, Seoul 02792, Republic of Korea
[b] Division of Energy and Environment Technology, KIST-School, University of Science and Technology, Seoul 02792, Republic of Korea
[c] Department of Materials and Energy Science and Engineering, Nelson Mandela African Institution of Science and Technology, P.O. Box 447, Arusha, Tanzania
[d] Department of Water and Environmental Science and Engineering, Nelson Mandela African Institution of Science and Technology, Arusha, P.O. Box 447, Tanzania

HIGHLIGHTS

- The performance of intercalating electrodes was systematically evaluated.
- The variations in intercalating materials by fabrication route were investigated.
- Study provides insights for maximizing electrochemical desalination performance.
- Study guides the development of various BDIs using faradaic materials.

ARTICLE INFO

Keywords:
Capacitive deionization
Asymmetric capacitive deionization
Battery deionization
Cell architecture
Energy efficiency

ABSTRACT

Capacitive deionization (CDI) is an alternative desalination technique for low-to-moderate salinity feeds. Despite significant advances in electrode material design, CDI's thermodynamic energy efficiency (*TEE*) remains low and has become important in assessing feasibility for real-world applications. Innovative cell configurations are key to improving *TEE*; however, their performance trends need to be contextualized, given the scattered information that can be challenging to compare. This study evaluates various desalination cells, including conventional CDI, single- and multi-channel asymmetric CDI, and multi-channel battery deionization (BDI). Using MoS_2 as a representative intercalating material, the position of active sites on composite electrodes was first optimized. Hydrothermally-grown MoS_2 on carbon nanofibers exhibited enhanced charge transfer compared to MoS_2 embedded in nanofibers. Among the tested configurations using 20 mM NaCl in single-pass mode and 50% water recovery, BDI demonstrated over 3.7 times higher *TEE* than asymmetric setups and 50 times higher than typical CDI while maintaining consistent desalination performance. BDI benefited from the combined effects of electrosorption/intercalation and ion exchange membranes in symmetric conformation, effectively utilizing charge. These findings provide insights into process engineering for improved electrochemical desalination and the enhancement of ion intercalation-based desalination configurations.

1. Introduction

Capacitive deionization (CDI) is an electrochemical water treatment technique used for desalinating low-salinity water (i.e., brackish water) or removing ionic substances [1]. Conventional CDI consists of two polarized electrodes that capture ions in the electric double layer (EDL) when voltage is applied and release them upon voltage removal or reversal [2]. The electrodes are the main components in a CDI setup, where carbons of varying structures have been most commonly used [3]. Novel variations of classical CDI, employing faradaic materials, have overcome various limitations associated with carbons (e.g., co-ion expulsion effect, carbon oxidation) and achieved high removal

* Corresponding author.
** Corresponding authors at: Center for Water Cycle Research, Korea Institute of Science and Technology, 5 Hwarang-ro 14-gil, Seongbuk-gu, Seoul 02792, Republic of Korea.
E-mail addresses: yusufu.jande@nm-aist.ac.tz (Y.A.C. Jande), jbyun@kist.re.kr (J. Byun), moonson@kist.re.kr (M. Son).

https://doi.org/10.1016/j.desal.2024.117857
Received 7 April 2024; Received in revised form 8 June 2024; Accepted 16 June 2024
Available online 20 June 2024

capacities [4]. Ion removal using faradaic materials occurs via reversible ion intercalation or conversion reactions, leading to better charge utilization since the ions are captured within the entire structure of the material rather than only at the surface [2,5]. Cation intercalation-type materials (often called faradaic- or battery-type materials) are the most studied and are usually composited with carbon materials to enhance charge transfer performance and dimensional stability [2,6].

Besides the material design perspective, the energy efficiency of CDIs is an important yet considerably less addressed aspect, which enables the assessment of their feasibility in practical applications [7]. In particular, the cell architecture of CDIs plays a significant role in enhancing thermodynamic energy efficiency (*TEE*), which is relatively lower than that of electrodialysis (ED) [8] and reverse osmosis (RO) [9,10]. Different architectures that have been explored include flow-through CDI [5,11], asymmetric CDI [12], flow-electrode CDI [13], and multi-channel setups that employ ion exchange membranes (IEMs) [14–16].

TEE in conventional CDIs is primarily hampered by the co-ion desorption effect [17], where ions of the same polarity as the electrode are desorbed as counter-ions are adsorbed. To minimize this phenomenon, IEMs [18,19], electrode surface-charge modification [20], and the use of permselective faradaic electrodes in asymmetric setups [12,21] have been applied, yielding enhanced charge efficiencies. However, there are issues of imbalanced ion storage in asymmetric setups due to dissimilar anode and cathode properties [22]. Flow-electrode CDI [23] may overcome these challenges but introduces additional energetic requirements for pumping electrode slurry and potential electrode clogging problems [24,25]. Multi-channel cell configurations involving synergistic ion electrosorption/intercalation into electrodes and ionic transport between channels through IEMs (similar to electrodialysis) may provide continuous water desalination at enhanced *TEE* levels. Such setups have been recently demonstrated using carbon electrodes [14,25,26] and faradaic electrodes [15,16,27]. While the evolution of configurations in CDIs holds promise, understanding performance trends proves challenging due to the abundance of scattered information. This difficulty arises from variations in test conditions and the use of non-standard metrics, making comparisons intricate. Thus, there is an urgent need for a systematic investigation of different setups to objectively compare CDI configurations.

Another important feature in composite faradaic electrodes is the location of active sites, which impacts intercalation kinetics and the long-term stability of the electrodes in electrochemical environments. This is primarily influenced by the fabrication route, where the active agent can be embedded in or surface-anchored on a carbon substrate [28]. An accurate comparison of cell configurations would be contingent upon using electrodes with optimally positioned active agents.

This study demonstrated the performance variation of ion intercalating materials among configurations and between fabrication routes. *TEE* was taken as the main desalination performance indicator among the setups examined. Using molybdenum disulfide (MoS_2) as a representative ion intercalation agent, systematic structural engineering was conducted through electrospinning and hydrothermal coatings to fabricate free-standing carbon composite electrodes. The effect of electrode structures on electrochemical performance was then systematically examined by varying the location of active agents. Enhanced stability and diffusion-controlled capacitance were attained with hydrothermally-grown MoS_2, in which majority of the active materials were involved in ion storage reactions. The desalination performance of hydrothermally-grown MoS_2 was evaluated in five different cell configurations, including conventional CDI, single- and multi-channel asymmetric CDI, and multi-channel battery deionization (BDI). The approach used in this study is anticipated to provide insights into process engineering for maximizing electrochemical desalination performance and to guide the development of various BDIs using faradaic materials.

2. Materials and methods

2.1. Materials

Polyacrylonitrile (PAN, average M_w = 150,000, Sigma-Aldrich, Korea), polyvinylpyrrolidone (PVP, average M_w = 1,300,000, Sigma-Aldrich, Korea), terephthalic acid (PTA, 98%, Sigma-Aldrich, Korea), mineral oil (light, Sigma-Aldrich, Korea), *N,N*-dimethylformamide (DMF, 99.8%, Sigma-Aldrich, Korea), and *n*-hexane (98%, Samchun Chemicals, Korea) were used in nanofiber fabrication. MoS_2 nanoparticles (90 nm, 99%, Sigma-Aldrich, Korea) were embedded into the nanofibers, while thiourea (CH_4N_2S, 99%, Sigma-Aldrich, Korea) and ammonium heptamolybdate tetrahydrate ($(NH_4)_6Mo_7O_{24}\bullet 4H_2O$, 98%, Sigma-Aldrich, Korea) were used for the hydrothermal synthesis of MoS_2 nanoflakes on carbon nanofibers. Electrolyte solutions were prepared in Millipore-grade deionized water (18.2 MΩ·cm) using sodium chloride (NaCl, 99%, Sigma-Aldrich, Korea), potassium chloride (KCl, 99%, Sigma-Aldrich, Korea), magnesium chloride hexahydrate ($MgCl_2{\cdot}6H_2O$, 99%, Sigma-Aldrich, Korea), and calcium chloride dihydrate ($CaCl_2{\cdot}2H_2O$, extra pure, Samchun Chemicals, Korea). Ethanol (95%, Samchun Chemicals, Korea) was used for washing samples. An anion exchange membrane (AEM, Selemion ASVN) and a cation exchange membrane (CEM, Selemion CMVN), were supplied by Asahi Glass, Japan.

2.2. Materials preparation

2.2.1. Fabrication of hollow carbon nanofibers

The fabrication of hollow carbon nanofibers (Fig. S1a: steps 1–6) was carried out using an electrospinning process with a NanoNC electrospinning system (ESR-200R2D) equipped with a coaxial nozzle. The core diameter of the nozzle was 0.5 mm, and the shell diameter was 1.26 mm (16G–21G). Briefly, a 13 wt% electrospinning solution was prepared from PAN, PTA, and PVP in a ratio of 7:2:1 in DMF. PAN served as the primary carbon source, PTA acted as a pore-forming agent, and PVP facilitated the embedding of MoS_2 in the nanofibers and provided nitrogen. The solution was homogenized by stirring for 14 h at 55 °C. The solution was then transferred into a 10 mL syringe and used as the shell solution during electrospinning at a flow rate of 1.0 mL h^{-1}. Mineral oil was used as the core solution at a flow rate of 0.3 mL h^{-1}. A voltage of 13.5 kV was applied between the nozzle and a flat aluminum collector placed 12 cm away. The electrospun nanofibers were then peeled off the collector, soaked in *n*-hexane for 12 h to extract the mineral oil, and dried in a fume hood. The dried hollow nanofibers were stabilized by heating in a muffle furnace at a ramp rate of 2 °C min^{-1} to 260 °C for 2 h. Finally, the nanofibers were carbonized in a tube furnace at 800 °C for 1 h under flowing nitrogen gas with a heating rate of 5 °C min^{-1}. The carbonized hollow nanofibers were denoted as NF.

2.2.2. Fabrication of hollow carbon nanofibers embedded with MoS_2

Hollow carbon nanofibers embedded with MoS_2 (Fig. S1b) were prepared by first dispersing 0.2 g of MoS_2 nanoparticles in 10 g of DMF and sonicating for 30 min. Using >0.2 g of MoS_2 resulted in clogging of the nozzle during the electrospinning process. PAN, PTA, and PVP were added to the DMF-MoS_2 mixture and stirred for 14 h at 55 °C. The resulting solution was then processed similarly to the NF carbonization procedure. The final product was denoted as NFME.

2.2.3. Hydrothermal coating with MoS_2

For the hydrothermal coating process (Fig. S1a: steps 7–10), the precursor solution for MoS_2 was prepared by dissolving 0.92 g of CH_4N_2S and 0.5 g of $(NH_4)_6Mo_7O_{24}\bullet 4H_2O$ in 20 mL of deionized water and stirring for 30 min at 25 °C. The prepared solution and a piece of NF with a diameter of 3.5 cm were then transferred into a 150 mL Teflon-lined hydrothermal reactor and kept in an oven at the required temperature (160 °C, 200 °C, or 230 °C) for 16 h. After natural cooling, the

samples were washed several times in deionized water and then in ethanol, and dried overnight. The as-prepared samples were denoted as NFM160, NFM200, and NFM230 according to the synthesis temperature.

2.3. Material structural analysis

The microstructure and elemental mapping of the fabricated materials were analyzed using a field emission scanning electron microscope (FE-SEM S-4200, Hitachi) equipped with an energy dispersive spectrometer (EDS). X-ray diffraction (XRD) with Cu Kα radiation ($\lambda = 1.541$ Å) was employed to examine the material's crystal structure (Rigaku DMax 2500/PC), while the chemical structure was investigated using X-ray photoelectron spectroscopy (XPS) with Al Kα (1486.6 eV) in a PHI 5000 VersaProbe Ulvac-PHI instrument. Fourier transform infrared (FT-IR) spectroscopy was conducted using an Agilent Cary 630. Nitrogen adsorption-desorption isotherms were measured at 77 K with a Micromeritics 3Flex adsorption analyzer. The electrodes' specific surface area was determined via the Brunauer-Emmett-Teller (BET) method, and pore size distributions were assessed using the Barrett-Joyner-Halenda (BJH) method. The interlayer spacing (d-spacing) in MoS_2 was calculated using Eq. (1) (Bragg equation) [29].

$$d\text{-}spacing = \frac{n\lambda}{2sin\theta} \tag{1}$$

where λ is the wavelength of the incident X-ray ($\lambda = 0.154$ nm), θ is the X-ray's angle of incidence (rad) to the corresponding plane, and n is the diffraction order ($n = 1$).

2.4. Electrochemical measurements

Cyclic voltammetry (CV) and electrochemical impedance spectroscopy (EIS) measurements were conducted using an electrochemical workstation (ZIVE SP1, WonATech Co., Ltd., Korea) with 1 M NaCl (unless otherwise stated) in a three-electrode setup consisting of the working electrode (as-prepared sample), reference electrode (Ag/AgCl), and counter electrode (pristine carbon nanofiber sheet). The electrolyte chamber measured 2 cm long × 3 cm diameter. CV scans were conducted at a scan rate of 1.0 mV s^{-1} within a potential window of −0.8 V to 0.8 V. EIS tests were performed across the frequency range of 100 kHz to 10 mHz with a perturbation amplitude of 5 mV. The specific capacitance (C_s, F g^{-1}) was determined from the CV curves using Eq. (2).

$$C_s = \frac{\int I\,dV}{2mv\Delta V} \tag{2}$$

where I is the response current (A), m is the mass of the working electrode (g), v is the scan rate (V s^{-1}), and ΔV is the applied potential window (V).

For determination of EDL-based (capacitive) and diffusion-controlled capacitances, CV was performed at 0.5, 1.0, and 1.5 mV s^{-1} in a potential window of −0.8 V to 0.8 V. Quantification was then done using Eq. (3) [30,31].

$$i(V) = i_{EDL} + i_{diffusion} = k_1 v + k_2 v^{1/2} \tag{3}$$

where $i(V)$ is the current at a particular voltage (V), i_{EDL} is the capacitive-controlled current, $i_{diffusion}$ is the diffusion-controlled current, and k_1 and k_2 are variable parameters that depend on the applied voltage.

2.5. Desalination cell configurations

The desalination cells were cylindrical chambers with an effective diameter of 3 cm (area = 7.07 cm^2) (Fig. S2). Symmetric CDI cells (Fig. 1a) utilized NF electrodes as both cathode and anode. The asymmetric CDI (ACDI) cell (Fig. 1b) utilized NF as the anode and a MoS_2-loaded electrode as the cathode. A CEM and an AEM were placed between the ACDI cells to create a three-channel ACDI (3-Ch ACDI) (Fig. 1c). The BDI cells contained MoS_2-loaded electrodes on either side, with the two-channel BDI (2-Ch BDI) (Fig. 1d) having an AEM in between, while the four-channel BDI (4-Ch BDI) (Fig. 1e) had 2 AEMs separated by a CEM between the electrodes. Graphite foils were used as current collectors. For all setups, fabric spacers and silicon rubber gaskets with adequately shaped water flow paths were placed between each component to maintain uniform flow and prevent leakage.

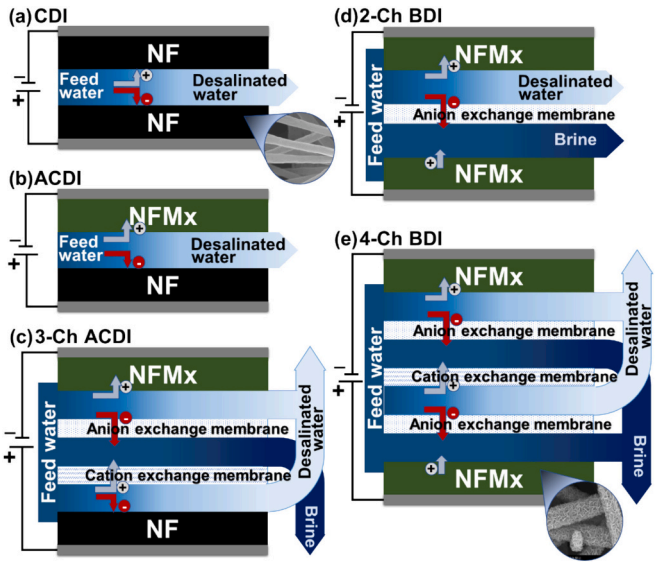

Fig. 1. Schematics of electrochemical cells for (a) conventional symmetric CDI, (b) ACDI, (c) 3-Ch ACDI, (d) 2-Ch BDI, and (e) 4-Ch BDI. NFMx indicates the MoS_2-loaded electrode, and x represents the synthesis temperature of MoS_2.

A single-pass operation mode was employed during the desalination experiments. The feed solution flowed through the cells at a rate of 0.5 mL min^{-1} or 1 mL min^{-1} without recirculation. Current and voltage supply and recording were conducted via a battery cycler (WBCS3000, WonATech Co., Ltd., Korea). A constant voltage of 0.8 V was applied for 5 min in CDI and ACDI tests to enable ion sorption, while desorption was achieved at 0 V for 5 min. For 3-Ch ACDI, a constant voltage of 0.8 V was applied for ion removal along the peripheral channels, and then it was reversed to −0.8 V for desalination in the central channel. In the BDI cells, a constant current density of 5 A m^{-2} was applied to increase the voltage to 0.8 V for intercalation in one electrode while the opposite electrode was deintercalating. Once 0.8 V was reached, the current was reversed (−5 A m^{-2}) with a terminal voltage of −0.8 V to cause a reversal in the actions of the electrodes. Effluent conductivity was continuously monitored and recorded per second using a flow-through conductivity meter (eDAQ, ET908, Australia).

The specific adsorption capacity (SAC, mg g^{-1}) was calculated using Eq. (4).

$$SAC = \frac{M\varnothing \int_0^{Tc} (C_0 - C_t)\,dt}{m_e} \tag{4}$$

where M is the molar mass of the solute (g mol^{-1}), $\varnothing$ is the flow rate (L s^{-1}), T_c is the charging time (s), C_0 is the feed concentration (mM), C_t is the concentration at time t (mM), and m_e is the electrode mass (g).

Charge efficiency (Λ, %) was calculated using Eq. (5).

$$\Lambda = \frac{F\varnothing \int_0^{Tc} (C_0 - C_t)\,dt}{1000 \int_0^{Tc} I\,dt} \tag{5}$$

F is the Faraday's constant (96,485.33C mol^{-1}), and I is the current (A).

The specific energy consumption (SEC, kWh m^{-3}) was calculated using Eq. (6).

$$SEC = \frac{\int_0^{Tc} VI\, dt}{3600 \varnothing T_c} \tag{6}$$

where V is the voltage (V).

The thermodynamic energy efficiency (TEE, %) was calculated using Eq. (7).

$$TEE = \frac{\Delta g}{SEC} \tag{7}$$

where Δg represents the specific Gibbs free energy of separation, determined according to Eq. (8) [5].

$$\Delta g = 2RT\left\{\frac{C_0}{\gamma} ln\left[\frac{C_0 - \gamma C_D}{C_0(1-\gamma)}\right] - C_D ln\left[\frac{C_0 - \gamma C_D}{C_D(1-\gamma)}\right]\right\} \tag{8}$$

R is the ideal gas constant (8.314463 J mol^{-1} K^{-1}), T is the absolute temperature (K), C_D is the average concentration of the product water (mM), and γ is the water recovery.

The maximum and average changes in solution concentration (ΔC_{max} and ΔC_{av}) were calculated using Eqs. (9) and (10), respectively.

$$\Delta C_{max} = C_0 - C_{low} \tag{9}$$

$$\Delta C_{av} = C_0 - C_D \tag{10}$$

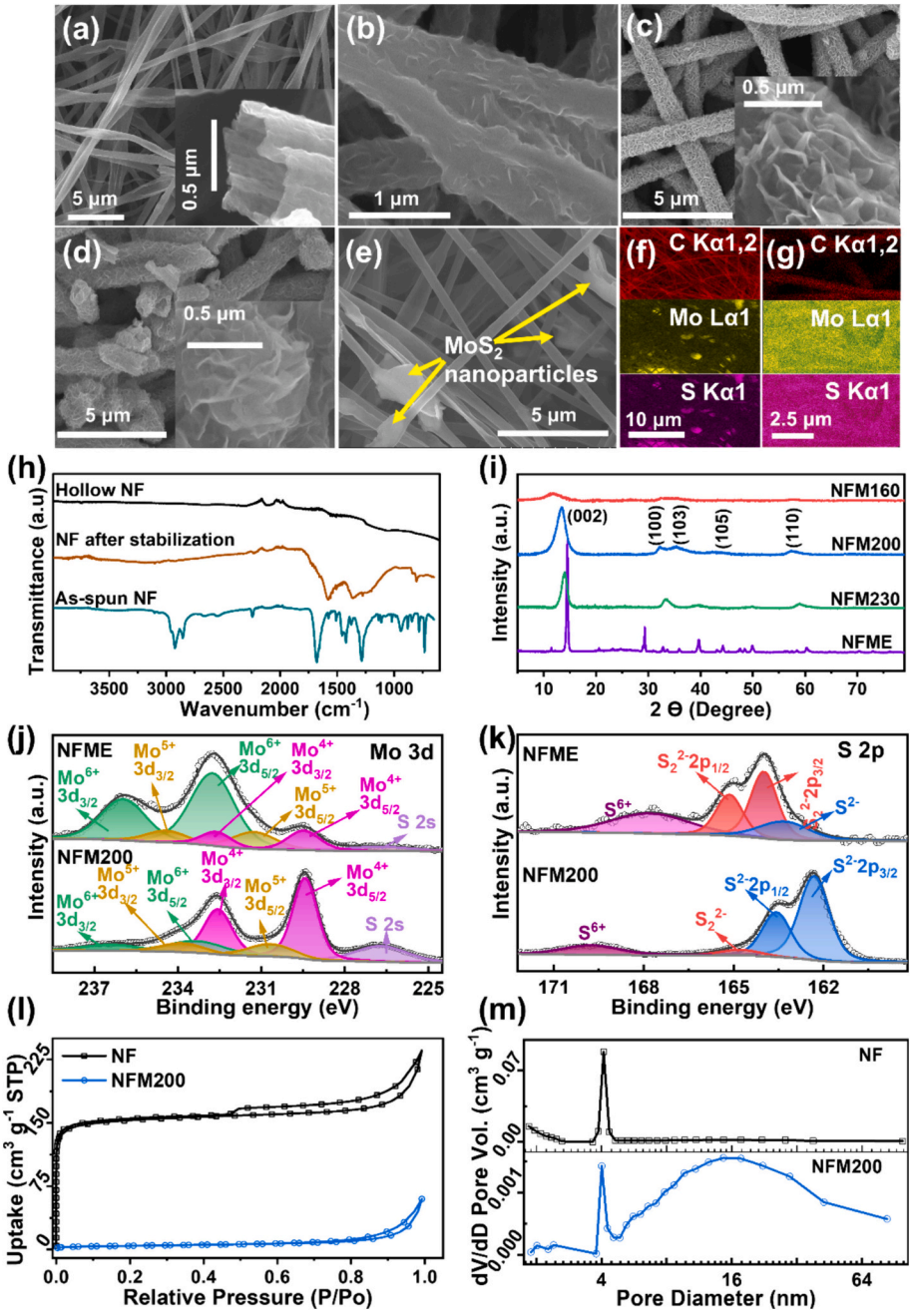

Fig. 2. FE-SEM images of (a) NF, (b) NFM160, (c) NFM200, (d) NFM230, and (e) NFME, and the corresponding EDS mappings of C, Mo, and S in (f) NFME and (g) NFM200. (h) FTIR spectra of the as-spun hollow NFs, the NFs after thermal stabilization, and the carbonized hollow NF. (i) XRD spectra of NFM160, NFM200, NFM230 and NFME. (j) Mo 3d and (k) S 2p XPS spectra of as-prepared NFME and NFM200. (l) N_2 sorption/desorption isotherms and (m) the pore-size distributions of NF and NFM200.

where, C_{low} is the lowest concentration (mM) of desalinated effluent.

3. Results and discussion

3.1. Physico-chemical properties of MoS_2-incorporated carbon nanofibers

The structural morphology of the as-spun nanofibers was analyzed by FE-SEM (Fig. 2a–e). From FE-SEM images, NF exhibited a random alignment of hollow fibers with slits, wrinkles, and pitted surfaces (Fig. 2a). The average nanofiber diameter was approximately 620 ± 95 nm. In comparison, the shell thickness measured 130 ± 30 nm. The rough surfaces and pits on the nanofibers resulted from the sublimation of PTA, which occurs around 300 °C [32], and the degradation of PVP [33] during the carbonization process. MoS_2 nanoflakes are uniformly positioned on the nanofiber surfaces. NFM160 (Fig. 2b) has the lowest density of nanoflakes due to slower nucleation at the lower temperature applied in the hydrothermal process [34], while NFM230 (Fig. 2d) is densely covered with some flower-like nanospheres sticking out. A few nanospheres are also created on the surface of NFM200 (Fig. 2c). Hydrothermally produced MoS_2 is known to cluster into dense spheres during synthesis [35]. However, the fibrous 3-D carbon network inhibited such agglomeration, resulting in the uniform anchoring of MoS_2 nanoflakes with the observed flower-like morphology. Higher temperatures can rapidly grow MoS_2 [34], leading to denser deposition and agglomeration into nanospheres, as seen with NFM230. These surface attributes among NFMs are critical as they determine the material's specific surface area and pore size distribution, directly influencing its specific capacitance and ionic transport [36]. NFME shows the embedded MoS_2 within the carbon nanofibers in a bead-on-string-like formation (Fig. 2e). The distribution of MoS_2 on NFME is relatively uneven, mainly due to particle-size differences, which are also noted on the EDS mapping (Fig. 2f). In contrast, the hydrothermally coated samples show a homogeneous distribution (Fig. 2g) owing to the gradual growth of particles on the carbon substrate. The structural transition from polymeric to carbonized nanofibers was evaluated using FTIR analysis (Fig. 2h and Text S1).

From XRD measurements (Fig. 2i), typical diffraction peaks for hexagonal MoS_2 were observed in NFMx and NFME, corresponding to the (002), (100), (103), (105), and (110) planes of pristine MoS_2 (Fig. S3a, JCPDS #01-077-1716). NFME exhibited narrow diffraction peaks depicting high crystallinity of the embedded MoS_2, while the hydrothermally processed samples had broader peaks. The diffraction peak associated with the (002) plane was shifted to a lower 2θ for the hydrothermally processed samples and was also seen to shift lower when the reaction temperature was reduced, suggesting increased interlayer spacing and lower crystallinity [34]. Based on the Bragg equation, the interlayer spacings corresponding to the (002) plane were determined to be 0.73, 0.66, 0.63, and 0.62 nm for NFM160, NFM200, NFM230, and NFME, respectively. Interlayer spacing was an important parameter as it would influence ion diffusion kinetics and cycle stability after repeated intercalation/deintercalation processes. NFME displayed additional peaks at 11.5° and 29.3° associated with MoO_3 [37], attributed to oxidation reactions occurring during thermal stabilization.

The chemical states of the as-prepared materials were identified using XPS, showing the presence of molybdenum (Mo), sulfur (S), carbon (C), nitrogen (N), and oxygen (O) elements (Fig. S3b). In the Mo 3d region (Fig. 2j), NFM200 shows the S 2 s peak at 226.7 eV, corresponding to S^{2-} in MoS_2 [38]. The doublet peaks at 229.4 eV and 232.5 eV are respectively attributed to Mo^{4+} $3d_{5/2}$ and Mo^{4+} $3d_{3/2}$ of MoS_2, while those at 233.3 eV and 236.4 eV are assignable to Mo^{6+} $3d_{5/2}$ and Mo^{6+} $3d_{3/2}$ orbitals in MoO_3 [34]. The doublet located at 230.7 eV and 233.8 eV corresponds to Mo^{5+} $3d_{5/2}$ and Mo^{5+} $3d_{3/2}$, which existed as intermediate sulfide phases (MoO_xS_y) due to the partial reduction of Mo^{6+} [34,39]. Similar Mo peaks were observed in NFME. However, NFME peaks corresponding to Mo^{6+} were stronger, while those associated with Mo^{4+} were weaker, indicating significant oxidation of surface MoS_2 to MoO_3 during the thermal stabilization of the nanofibers in air. In the S 2p region (Fig. 2k), NFM200 showed a doublet at 162.3 eV and 163.5 eV, which corresponded to S^{2-} $2p_{3/2}$ and S^{2-} $2p_{1/2}$ of MoS_2, respectively, and a peak at 164.8 eV attributable to bridging S_2^{2-} and/or apical S^{2-} ligands [40]. The peak at higher binding energy (169.7 eV) was attributable to S^{6+} [41]. NFME showed the S 2p peaks at 163.8 eV, 164 eV, 165.2 eV, and 169.5 eV, which were assignable to S^{2-}, S_2^{2-} $2p_{3/2}$, S_2^{2-} $2p_{1/2}$, and S^{6+}, respectively [39,41]. The S^{6+} peak was broader and stronger in NFME, signifying more extensive oxidation than in NFM200. These surface characteristics provided a clue to the importance of electrode fabrication routes, especially when involving thermal processes in air using bulk active agents.

From nitrogen physisorption measurements at 77 K, the pristine NF exhibited a *type IV* isotherm with a hysteresis loop (Fig. 2l), indicating the coexistence of micropores and mesopores, essential properties for enhanced mass transfer and better access to active sites for electrochemical applications [42,43]. In contrast, NFM200 showed a *type III* isotherm after the surface loading of MoS_2 on the NF. NF exhibited a high BET-specific surface area of 471.94 $m^2\ g^{-1}$ and a total pore volume of 0.317 $cm^3\ g^{-1}$, while NFM200 showed a greatly reduced surface area of 16.27 $m^2\ g^{-1}$ and a total pore volume of 0.054 $cm^3\ g^{-1}$. The high porosity of NF resulted from the hollow and highly pitted structure, as observed in the SEM images. In contrast, the hydrothermal process resulted in a dense fibrous structure in NFM200 where the hollow core was filled, and most of the carbon pores and pits were covered by the MoS_2 nanoflakes, such that a majority of the accessible surface and volume were occupied by the anchored MoS_2. The BJH pore size distribution profiles (Fig. 2m) showed that both NF and NFM200 shared narrow mesopores at 4 nm. However, NFM200 had a substantial proportion of larger mesopores (>6 nm) due to the decorative arrangement of nanoflakes on the carbon nanofibers. This feature would enhance electrochemical activity arising from the well-distributed active sites for ion intercalation and a hierarchical pore structure promoting unhindered ionic transport and EDL formation [44].

3.2. Electrochemical performance

3.2.1. Electrochemical properties and ion storage mechanisms

During CV experiments operated under NaCl electrolyte at a scan rate of 1 mV s^{-1} (Fig. 3a), NF exhibited an almost rectangular CV shape, indicating typical EDL-controlled capacitance [1]. In contrast, the MoS_2-loaded NF electrodes had leaf-shaped CV profiles indicative of mixed EDL capacitance and intercalation pseudocapacitance. Mild bumps were also noticeable on the curves of electrodes containing MoS_2, attributed to increased interaction between MoS_2 and Na^+ at the nanopore level at the low scan rate [31]. Deviation in the mild redox peak positions among the MoS_2-loaded samples was also observed. This deviation is likely caused by the different interlayer sizes of the MoS_2, varying proportions of carbon and MoS_2 in the electrodes, and/or the presence of minor impurities, whose effects were largely magnified by the low scan rate applied. Regarding plot size, NFM200 had the most prominent CV curve, indicating superior capacitance and better ion storage capacity.

A systematic analysis of the CV curves at varying scan rates was performed based on the relationship between the scan rate and the response current, as shown in Eq. (3), to differentiate capacitive and diffusion-controlled contributions to the overall capacitance. Generally, for a pseudocapacitive material, the total response current during CV is due to a contribution of surface-controlled/capacitive and diffusion-controlled processes. A capacitive process occurs when the response current at a particular voltage varies linearly with the scan rate. In contrast, a diffusion-controlled process occurs when the current is proportional to the square root of the scan rate [30,31]. For example, NFM200 exhibited varying proportions of capacitive and diffusion-controlled response currents at a scan rate of 1 mV s^{-1}, where surface-controlled current appears dominant (Fig. 3b). Among the electrodes tested, NFM200 possessed the highest total specific capacitance of

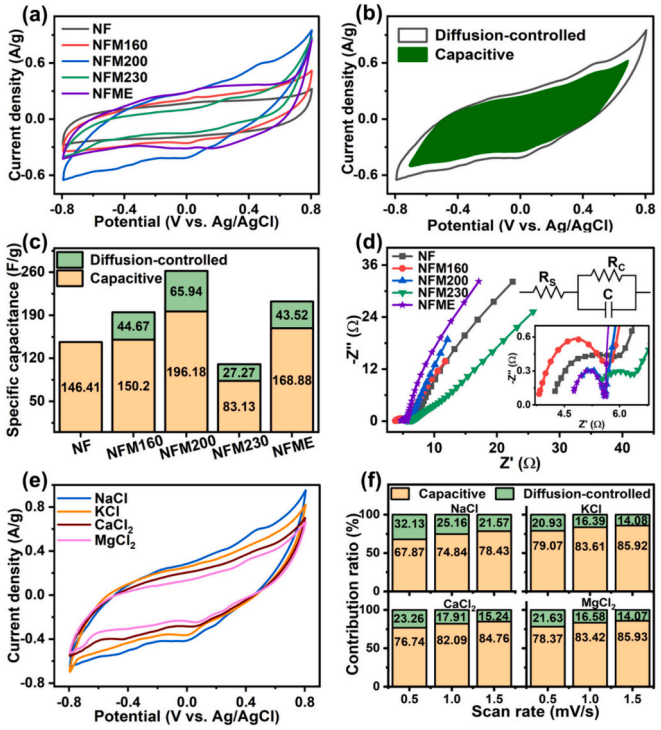

Fig. 3. (a) CV curves of the electrodes, (b) representation of the portions of capacitive and diffusion-controlled currents of NFM200, (c) capacitive and diffusion-controlled capacitance of the electrodes at 1 mV s^{-1}, (d) Nyquist plots of the electrodes (inset: zoomed in the high-frequency region), (e) CV curves of NFM200 in different 1 M electrolytes at 1 mV s^{-1}, and (f) capacitance contribution comparison for NFM200 in different electrolytes.

262.12 F g^{-1} and the largest proportion of diffusion-controlled capacitance at 25.16% (Fig. 3c). This resulted from the larger content of anchored MoS_2 particles on the carbon nanofibers compared to NFM160 and NFME, and also due to a favorable interlayer spacing as determined using XRD, which facilitated better diffusion of ions compared to NFM230. The lowest specific capacitance of NFM230 (110.4 F g^{-1}) could be attributed to a highly dense surface and a smaller interlayer spacing in the MoS_2 that constrained ion intercalation [45]. NFME with the embedded MoS_2 exhibited low diffusion-controlled capacitance due to the reduced accessibility of MoS_2. However, it benefitted from the highly porous carbon structure to have higher EDL-dominant specific capacitance compared to NFM160 and NFM230.

Nyquist plots from EIS tests (Fig. 3d) were used to evaluate the electrochemical resistance characteristics of NFMx and NFME. All electrodes exhibited similar plot shapes with a semicircle in the high-frequency region (related to charge transfer resistance at the electrode/electrolyte interface) and a slanting line in the low-frequency region (related to ion diffusion at the electrode's surface). NFM200 had the smallest semicircle and a steeper short slope, indicative of enhanced charge transfer capacity and faster ionic diffusion rates. The smaller semicircle could be ascribed to a relatively balanced structure between NF and MoS_2, providing charge conductivity and well-distributed active sites for enhanced charge transfer performance [38]. Additionally, the micro-mesoporous structure of NFM200 facilitated faster ionic transport. In contrast, NFM230 showed a distinctly low slope compared to the other samples, which was attributed to highly stacked MoS_2 nanoflakes slowing down the ionic transport. Overall, NFM200 performed optimally in the electrochemical tests due to its structural and compositional attributes. The hierarchical pore size distribution of NFM200 promoted unhindered ion transport, with the accessible MoS_2 nanoflakes serving as active sites on the surface for faster surface kinetics. The balance between NF and MoS_2 was critical for achieving the appropriate crystal structure of MoS_2 and sufficient electrical conductivity from NF, consequently promoting charge transfer. The performance of NFM200 demonstrates the importance of active site design for composite faradaic electrodes.

NFM200, with a high proportion of diffusion-controlled capacitance, was further evaluated in additional CV analyses using 1 M KCl, $CaCl_2$, and $MgCl_2$ electrolytes with different cation sizes. Except for varying integrated areas, similarly shaped CV curves (Fig. 3e) were obtained in the tested electrolytes, signifying similar processes occurring during CV cycling. The calculated total specific capacitance values were 262.12 F g^{-1} (NaCl), 224.77 F g^{-1} (KCl), 214.93 F g^{-1} ($CaCl_2$), and 175.08 F g^{-1} ($MgCl_2$) (Fig. 3f). The proportions of diffusion-controlled capacitance increased with a decrease in scan rate in all electrolytes due to the higher probability of ions for intercalation on the electrode at lower scan rates. Generally, the capacitive contribution was dominant, and advantageous for rapid ion storage in desalination applications [35]. Considering the relatively higher specific capacitance of NFM200 in NaCl electrolyte, it can be concluded that intercalation of Na^+ in MoS_2 was faster and kinetically more favorable. The relatively lower performance of $CaCl_2$ and $MgCl_2$ could be attributed to the divalent nature of the salts, leading to increased interactions with MoS_2 and sluggish diffusion kinetics [46]. Understanding the effects of these cations further elucidates the contribution of surface-anchored MoS_2 in the composite electrode. The stability of the intercalation electrodes in electrochemical environments was analyzed using CV as described in Text S2 and illustrated in Figs. S4 and S5. Accordingly, NFM200 was selected for subsequent desalination tests with different cell configurations, considering its higher specific capacitance, a larger proportion of diffusion-controlled activity, and fair electrochemical stability.

3.3. Desalination performance

3.3.1. Symmetric and asymmetric CDI configurations

Various desalination tests were conducted in constant voltage single-pass conditions using a 20 mM NaCl feed solution under CDI, ACDI, and 3-Ch ACDI configurations (Fig. 4a). NFM200 served as a cathode in the ACDI setups. A very low desalination extent was observed for symmetric CDI, with the sole NF electrode showing an ΔC_{max} of 0.9 mM at 0.5 mL min^{-1}; ACDI and 3-Ch ACDI exhibited higher ΔC_{max} values of 3.8 mM and 10.8 mM, respectively. Since the effluent concentration was not constant over the charging duration in these setups, ΔC_{av} were much lower at approximately 0.6 mM, 1.7 mM, and 4.9 mM for CDI, ACDI, and 3-Ch ACDI, respectively. Typical current profiles (Fig. 4b) in constant voltage experiments were exhibited by the three configurations of CDI, ACDI, and 3-Ch ACDI. The calculated *SAC* and Λ (Fig. 4c and d, respectively) followed the order of 3-Ch ACDI > ACDI > CDI (e.g., 79.9% > 69.3% > 21% for Λ, respectively). The low performance of conventional CDI configuration was due to unwanted charge utilization by co-ion desorption and the limited capacity of NF, which relied solely on the EDL for ion capture. The obtained *SAC* was also lower than most values reported in the literature for carbon materials due to the low applied voltage (0.8 V) compared to the commonly used voltage (1.2 V). An improved performance was observed in ACDI because of the higher capacity cathode (NFM200), which could capture Na^+ capacitively on the surface and intercalate it into the interlayer space of MoS_2. Simultaneously, Cl^- was electrosorbed on the carbon anode. The asymmetric nature of the cell and preferential selectivity of MoS_2 for cations also minimized co-ion desorption at the cathode, leading to improved *SAC* and Λ. The higher *SAC* in 3-Ch ACDI was certainly due to the combined effects of intercalation and electrosorption processes similar to ACDI. In addition, effective ion separation across the CEM and AEM in the multi-channel ACDI resulted in ion-rich and desalinated streams separated by the membranes. A higher Λ could also be achieved due to reduced co-ion desorption at the cathode and the extra channel containing expelled ions.

Likewise, the calculated *SEC* (Fig. 4e) and *TEE* (Fig. 4f) followed the

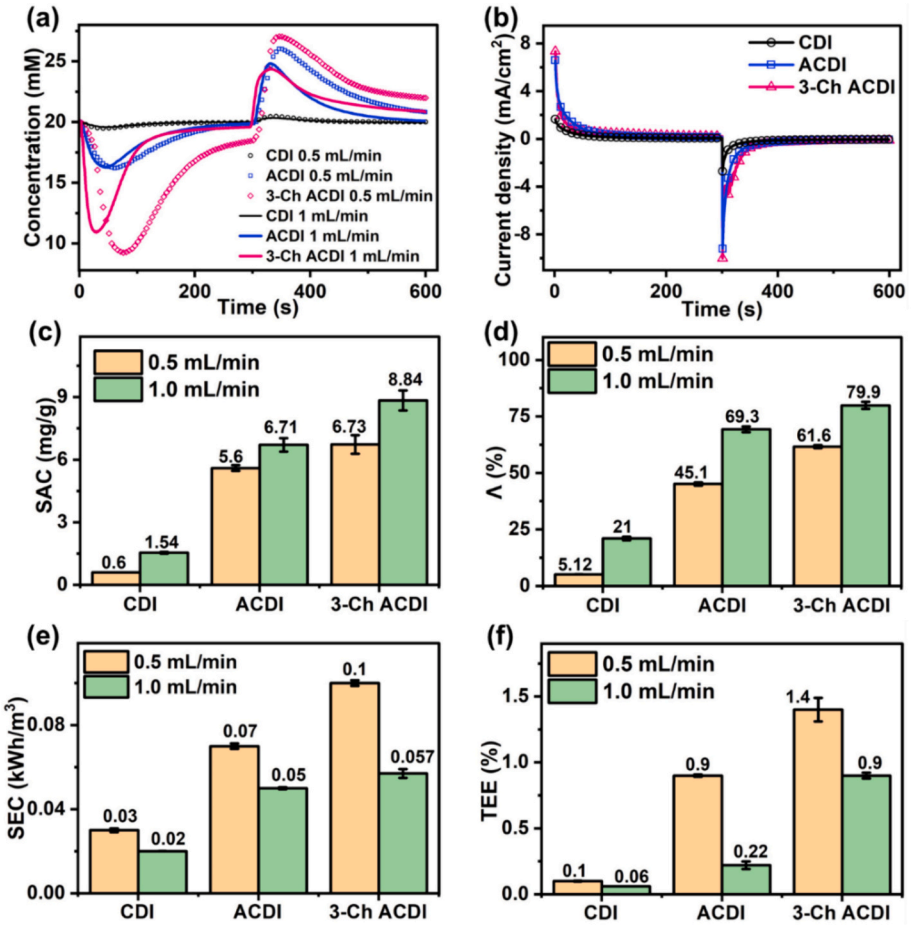

Fig. 4. (a) Representative desalination and (b) current density profiles (1 mL min^{-1}) of the different configurations in constant voltage (0.8 V) mode with NFM200. (c) Specific adsorption capacity (*SAC*), (d) charge efficiency (Λ), (e) specific energy consumption (*SEC*), and (f) thermodynamic energy efficiency (*TEE*) comparison of the different configurations.

order of 3-Ch ACDI > ACDI > CDI (e.g., 0.06% > 0.22% > 0.9% for *TEE*, respectively). The lower *SEC* in CDI was primarily due to low current density at constant voltage operation caused by high resistance and reactions occurring at the plain electrode. Additionally, parasitic consumption of applied charge in co-ion desorption led to an extremely low *TEE* since a very small ΔC_{av} could be attained. In ACDI and 3-Ch ACDI, high current density due to faradaic activity was the likely cause of the increased consumed energy. More importantly, *TEE* was improved due to the higher ΔC_{av}; this demonstrates the importance of cell configuration in achieving higher energy efficiency for CDIs.

3.3.2. *Battery deionization configurations*

The superior performance of ACDI with the combination of NFM200 and IEMs prompted the evaluation of the electrode in BDI configuration with constant current operation (Fig. 5a). After applying a constant current (±5 A m^{-2}), a decrease in effluent conductivity occurred in the desalination channel, while it increased in the salination channel and reached a constant value maintained until the set terminal voltage of ±0.8 V was reached and reversed. The 4-channel BDI cell exhibited a larger degree of salt removal with an ΔC_{av} of 6.5 mM at 0.5 mL min^{-1} and 3.8 mM at 1 mL min^{-1}. In contrast, 2-Ch BDI maintained an ΔC_{av} of 3.8 mM at 0.5 mL min^{-1} and 2.7 mM at 1 mL min^{-1}. The desalination step durations at 1 mL min^{-1} were ~12 and 9 min for 2-Ch BDI and 4-Ch BDI, respectively. The shorter duration in 4-Ch BDI resulted from the larger ohmic (iR) drop and higher overall cell resistance (higher slope) (Fig. 5b), leading to a smaller usable voltage window. The additional IEMs and complexity in cell assembly likely contributed to increased ohmic resistances in the 4-Ch BDI cell. Nevertheless, more IEMs/channels could yield a larger ΔC_{av} due to increased influent retention time per channel as the flow rate and applied current density remained unchanged. As expected, 4-Ch BDI had higher *SAC* and Λ compared to 2-Ch BDI (Fig. 5c and d, respectively). The enhanced *SAC* was mainly due to the greater ΔC_{av} in the 4-channel cell without any change in electrode mass; this was also the case for Λ, where more ions were removed while current density remained constant. The *SEC* in both setups (Fig. 5e) was fairly comparable at the higher flow rate but slightly higher in 4-Ch BDI at 0.5 mL min^{-1}. Generally, the higher resistance at constant current due to more water streams and IEMs in 4-Ch BDI implied an increased *SEC*. This effect became more pronounced because of depleted ions in the cell when the flow rate was reduced, increasing the overall resistance. Nevertheless, as for *TEE* (Fig. 5f), 4-Ch BDI yielded a higher value (2.99%) than 2-Ch BDI (1.78%) because of the considerably larger ΔC_{av}, corresponding to a larger Gibbs free energy of separation per volume of produced water [5].

The effect of flow rate in all configurations was notable. Increased flow rate caused increased *SAC* and Λ while reducing ΔC_{av}, *SEC*, and *TEE*. The increased *SAC* and Λ were attributed to increased delivered ions and improved removal kinetics facilitated by mass ion transfer. However, a faster flow rate reduced the ions' retention time in the cell, hence decreasing ΔC_{av} and *TEE*. Nevertheless, an increasing flow rate indicates a larger volume of processed water, leading to reduced energy consumed per unit of water.

Cyclic voltammetry revealed faster diffusion kinetics between NFM200 and Na^+. To verify this in a desalination setup, tests were carried out using NaCl, KCl, $CaCl_2$, and $MgCl_2$ in a 2-Ch BDI cell with NFM200 as the electrodes. Two sets of solutions were prepared: the first

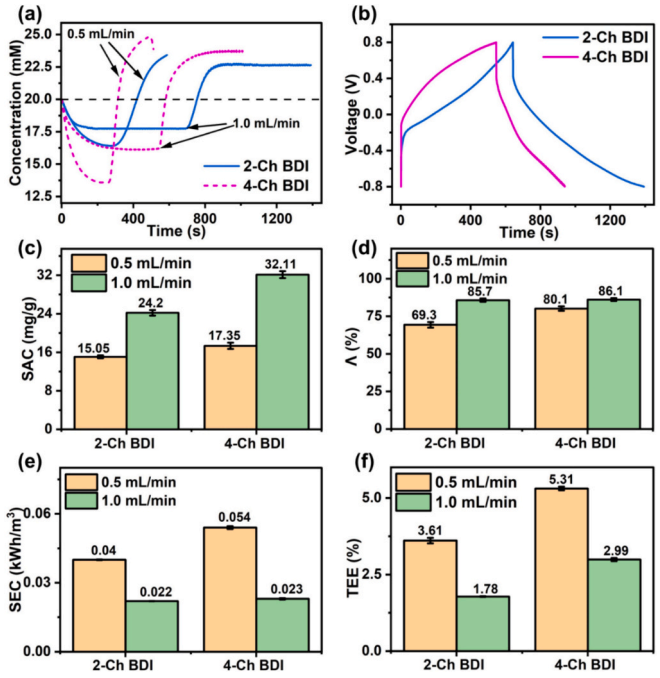

Fig. 5. (a) Representative desalination and (b) voltage profiles (1 mL min^{-1}) of 2-Ch BDI and 4-Ch-BDI at a constant current density of 5 A m^{-2} and cutoff voltage of ±0.8 V. (c) Specific adsorption capacity (*SAC*), (d) charge efficiency (*Λ*), (e) specific energy consumption (*SEC*), and (f) thermodynamic energy efficiency (*TEE*) comparison of the setups.

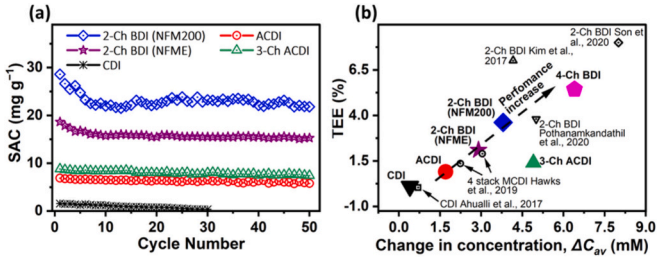

Fig. 6. (a) Specific adsorption capacity (*SAC*) stability over 50 cycles of 2-Ch BDI (NFM200 and NFME), ACDI (NFM200), 3-Ch ACDI (NFM200), and CDI (NF). (b) Thermodynamic energy efficiency (*TEE*) versus changes in solution concentration (ΔC_{av}) of the different configurations with a comparison of other works from the literature at a productivity of (~40–50 L h^{-1} m^{-2}).

set with the salt solutions at the same electrical conductivity, and the second set with equal concentration. It should be noted that this was not a selectivity test as the different salt solutions were not mixed. The desalination profiles (Fig. S6a and b) showed the highest desalination extents with NaCl in both instances. The rate of decrease in solution concentration (gradient of desalination profile at the start) in the equimolar set of solutions (Fig. S6b) was high for both NaCl and KCl, implying a more rapid uptake of the monovalent cations by the electrode. Considering the faster and higher extent of desalination by NFM200 with NaCl, it was evident that the intercalation/deintercalation of Na^+ in MoS_2 was kinetically more favorable than K^+, Ca^{2+}, and Mg^{2+}. This was likely due to its monovalent nature and more negative intercalation energy compared to K^+ [38,47]. Better extents of desalination were also observed with KCl than with $CaCl_2$ or $MgCl_2$, which could be attributed to a smaller hydrated ionic radius in K^+ [48] and a lower dehydration energy required for its partial dehydration during intercalation [49]. Additionally, the divalent nature of Ca^{2+} and Mg^{2+} caused slower ion mobility due to more interactions with MoS_2 [46]. Thus, increased charge density in multivalent ions could be a deterrent factor slowing down ion intercalation, while the hydrated ionic radii size, dehydration energy, and intercalation energy are important factors affecting cation intercalation kinetics in MoS_2 [38,46,50].

3.3.3. *Performance evaluation in various cell configurations*

Even with NFM200 as a representative faradaic material, notable variations in desalination efficiency were observed upon changing the cell configurations. For a fair evaluation of performance among the configurations, cycling stability and *TEE* of the electrodes were investigated under consistent experimental conditions. In a typical 2-Ch BDI cell, the desalination cycling test of NFM200 displayed a slight reduction in *SAC* from ~30 mg g^{-1} to ~20 mg g^{-1} over the first nine cycles before stabilization (Fig. 6a). This could be attributed to slower deintercalation of Na^+ during the initial intercalation/deintercalation cycles (i.e., not all intercalated Na^+ could be deintercalated during discharge), leading to quick electrode saturation in the ensuing cycles due to incomplete electrode discharge. The consequence was a decreasing *SAC* because of shorter successive charging durations, where charging time gradually decreased by several seconds each subsequent cycle. The *SAC* gradually stabilized after about the 9th cycle with a tendency to increase. It is believed that with repeated intercalation/deintercalation cycles, there was an expansion of the MoS_2 interlayer spacing, which alleviated mechanical strain, enhanced access to active sites, and enabled easier and more rapid mobility of Na^+ in and out of the interlayer space, leading to a more stabilized *SAC* as observed for the rest of the cycles [48]. Such structural expansion of MoS_2 has been previously reported by Chen et al. [51] and Srimuk et al. [52]. A control test using NFME showed similar stabilized performance but a smaller SAC reduction in the initial cycles, likely due to minimized MoS_2 layer expansion by the surrounding carbon structure. The *SAC* of NFME gradually declined over cycles, attributed to the surface oxidation and co-ion desorption of the exposed carbon layers as the main active sites. The performance of NFM200 in asymmetric setups showed relatively stable *SACs* from the start but lost approximately 16.1% and 15.7% of the original values for ACDI and 3-Ch ACDI, respectively, after the 50th cycle. An oxidized anode mainly caused the capacity decay in ACDI and 3-Ch ACDI due to inevitable carbon oxidation. Nevertheless, no inversion occurred as in the CDI cell of sole NF (Fig. S7), which exhibited a gradual reduction in ΔC_{av} over time and an eventual inversion of the electrosorption and desorption cycles due to rapid carbon oxidation. These cycle stability tests help discern the long-term usability and reliability of the intercalating material in relation to the configuration used.

To comprehensively understand the impact of CDI configurations on desalination performance, the trend in *TEE* of the various configurations was evaluated as a function of ΔC_{av} at a productivity of ~43 L h^{-1} m^{-2} (Fig. 6b), with a comparison of data from the literature with similar productivity (~40–50 L h^{-1} m^{-2}). Comprehensive data from more configurations are provided in Table S1, including typical approaches like MCDI with lower *TEE* (<3%). Throughout the literature, improved *TEE* in MCDI is noted only when there is an increase in cell stacks or significantly lower productivity. Two-channel BDIs exhibit high performance, with *TEE* between 3 and 15% at productivities up to ~43 L h^{-1} m^{-2}. Our systematic analysis across various configurations shows that *TEE* was in the order 4-Ch BDI (5.43%) > 2-Ch BDI (NFM200) (3.61%) > 2-Ch BDI (NFME) (2.1%) > 3-Ch ACDI (1.4%) > ACDI (0.9%) > CDI (0.1%) when tested under consistent conditions. This finding signifies more efficient energy utilization with intercalation electrodes by controlling the cell symmetry and using multiple channels. The location of active sites on the electrode also plays a critical role in enhancing the diffusion-controlled activity, with a three-fold higher *TEE* observed in NFM200 compared to NFME in an identical 2-Ch BDI setup. Additionally, the effect of more IEMs is evident in the >47% higher *TEE* in 4-Ch BDI than in 2-Ch BDI. A similar trend was reported by Kim et al. [16] using copper hexacyanoferrate electrodes where an 81% and 123% increase in *TEE* were realized by increasing the channels to four and six, respectively. Along with the number of IEMs, flow channel dimensions,

and separation stages are configuration-based factors that can influence *TEE* in BDI and result in varying values even for the same materials [53].

As for the material perspective, the fabrication route of carbon composite electrodes significantly influenced the performance of active materials. Compounds like bulk MoS_2 are particularly sensitive to fabrication processes involving high temperatures in air [54], as observed in NFME. Additionally, the amount of active materials embedded in host carbon is limited depending on the complexity of the fabrication process. Therefore, convenient processes such as hydrothermal coating could be preferable as they offer advantages in controlling the structural distribution and the number of active sites. Importantly, there is a need to rule out unwanted surface oxidation reactions that can alter the material's structure, requiring an optimal balance in composition between carbon and active material.

In terms of cell architecture, multi-channel configurations with a cation intercalation electrode in both symmetric and asymmetric setups resulted in enhanced *TEE*. The effect of uneven electrode chemistry and capacity in asymmetric configurations was significant in determining the cell's Λ and ΔC_{av}, which directly influence *TEE*. For BDI, a balanced electrode configuration and minimal co-ion desorption yielded high Λ and ΔC_{av}, which could be further increased by increasing the channels to achieve a higher *TEE*. Considering the typical examples of MoS_2 electrodes ever reported with relatively high *SAC*s and Λs (Table S2), it is envisioned that a higher *TEE* would be possible if their setups were hybridized with IEMs. However, the number of IEMs in the system should be selected elaborately as it directly influences the cell's ohmic resistance, determining the effective voltage window [16]. Therefore, to achieve optimal desalination performance with intercalating materials, a BDI configuration with an appropriate number of multi-channels would be the most effective approach, where the cost of IEMs and energy aspects of the entire system should be well balanced.

Considering the relatively rapid diffusion kinetics with monovalent cations (Na^+ and K^+), NFM200 may be a promising material for the electrochemical extraction of valuable ionic species such as Li^+ from aqueous sources. As already reported in the literature, the use of selective electrodes in CDI to separate Li^+ and various cations has great potential for practical application [55–57]. Enhanced cation selectivity in NFM200, for instance, can be achievable by tailoring charge cycle durations (relatively short cycles) to target rapid monovalent cation uptake while preventing ion exchange between multivalent and monovalent cations that occur with lengthy charge durations [49].

4. Conclusion

In conclusion, this study aimed to systematically evaluate the performance of intercalating electrodes in different CDI-based desalination configurations, including conventional CDI, single- and multi-channel ACDI, and multi-channel BDI. Composite carbon electrodes with MoS_2 were fabricated via electrospinning and hydrothermal coating to control the surface attributes of the electrodes (e.g., the location and the number of active sites). *TEE* served as an overall performance indicator in evaluating the desalination configurations as it considers both the amount of ions removed and the energy consumed. The main conclusions are as follows:

- A higher diffusion-controlled activity was achieved when the MoS_2 nanoflakes were hydrothermally grown on the surface of carbon nanofibers at 200 °C, resulting in a specific capacitance of 262.12 F g^{-1}. The balance between nanofiber and MoS_2 provided hierarchical porosity to promote ion transport and accessible active sites for faster charge transfer.
- Despite using the same intercalating electrode, significant discrepancies in desalination efficiency were observed when altering cell configurations. Among the examined configurations, 4-Ch BDI demonstrated a *TEE* of 5.43%, over 50 times higher than conventional CDI (0.1%) and 1.5 times higher than 2-Ch BDI (3.61%). While *TEE* in 3-Ch ACDI (1.4%) improved by 55% compared to single-channel ACDI (0.9%), it was 3.9 times lower than in 4-Ch BDI and 2.6 times lower than in 2-Ch BDI. These findings underscore the superior energy efficiency of symmetric multi-channel BDIs in desalination.
- Therefore, integrating faradaic desalination electrodes with IEMs can emerge as the optimal strategy for enhancing energy efficiency and boosting the competitiveness of CDI technology. To further enhance *TEE*, future endeavors could prioritize optimizing operational conditions, such as water recovery, which directly influences cell resistance in multi-channel cells.

CRediT authorship contribution statement

Bethwel Kipchirchir Tarus: Writing – review & editing, Writing – original draft, Visualization, Validation, Investigation, Formal analysis, Data curation, Conceptualization. **Zahid Ullah:** Writing – review & editing. **Yusufu A.C. Jande:** Writing – review & editing. **Karoli N. Njau:** Writing – review & editing. **Jeehye Byun:** Writing – review & editing, Writing – original draft, Visualization, Validation, Supervision, Conceptualization. **Moon Son:** Writing – review & editing, Writing – original draft, Visualization, Validation, Supervision, Funding acquisition, Conceptualization.

Declaration of competing interest

The authors declare that they have no known competing financial interests or personal relationships that could have appeared to influence the work reported in this paper.

Data availability

Data will be made available on request.

Acknowledgments

This work was supported by a National Research Foundation of Korea (NRF) grant funded by the Korean government (MSIT) [grant number 2021R1C1C2005643], the institutional programs of KIST [grant numbers 2E33081 and 2E33098], the International Center of Insect Physiology and Ecology (ICIPE) [World Bank financing agreement no. D347-3A] and the World Bank [Korea Trust Fund agreement no. TF0A8639] for the Partnership for Skills in Applied Sciences, Engineering, and Technology (PASET) Regional Scholarship and Innovation Fund.

Appendix A. Supplementary data

Supplementary data to this article can be found online at https://doi.org/10.1016/j.desal.2024.117857.

References

[1] C. Chen, A. Liu, C. Fei, B. Hui, Y. Li, D. Guan, D. Ju, High-performance nitrogen-doped porous carbon electrode materials for capacitive deionization of industrial salt-contaminated wastewater, Desalination 565 (2023) 116863.
[2] L. Wang, Y. Zhang, K. Moh, V. Presser, From capacitive deionization to desalination batteries and desalination fuel cells, Curr. Opin. Electrochem. 29 (2021) 100758.
[3] B. Han, G. Cheng, Y. Wang, X. Wang, Structure and functionality design of novel carbon and faradaic electrode materials for high-performance capacitive deionization, Chem. Eng. J. 360 (2019) 364–384.
[4] Q. Li, Y. Zheng, D. Xiao, T. Or, R. Gao, Z. Li, M. Feng, L. Shui, G. Zhou, X. Wang, Z. Chen, Faradaic electrodes open a new era for capacitive deionization, Adv. Sci. 7 (2020) 2002213.
[5] M. Son, V. Pothanamkandathil, W. Yang, J.S. Vrouwenvelder, C.A. Gorski, B. E. Logan, Improving the thermodynamic energy efficiency of battery electrode deionization using flow-through electrodes, Environ. Sci. Technol. 54 (2020) 3628–3635.
[6] M. Gao, W. Liang, Z. Yang, T. Ao, W. Chen, Flexible ultrathin nitrogen-doped carbon mediates the surface charge redistribution of a hierarchical tin disulfide

nanoflake electrode for efficient capacitive deionization, J. Colloid Interface Sci. 650 (2023) 1244–1252.
[7] S.A. Hawks, A. Ramachandran, S. Porada, P.G. Campbell, M.E. Suss, P. M. Biesheuvel, J.G. Santiago, M. Stadermann, Performance metrics for the objective assessment of capacitive deionization systems, Water Res. 152 (2019) 126–137.
[8] S.K. Patel, M. Qin, W.S. Walker, M. Elimelech, Energy efficiency of electro-driven brackish water desalination: electrodialysis significantly outperforms membrane capacitive deionization, Environ. Sci. Technol. 54 (2020) 3663–3677.
[9] M. Qin, A. Deshmukh, R. Epsztein, S.K. Patel, O.M. Owoseni, W.S. Walker, M. Elimelech, Comparison of energy consumption in desalination by capacitive deionization and reverse osmosis, Desalination 455 (2019) 100–114.
[10] S.K. Patel, C.L. Ritt, A. Deshmukh, Z. Wang, M. Qin, R. Epsztein, M. Elimelech, The relative insignificance of advanced materials in enhancing the energy efficiency of desalination technologies, Energ. Environ. Sci. 13 (2020) 1694–1710.
[11] L. Wang, Z. Liu, Z. Wang, Q. Ma, Z. Guo, G. Shen, K. Wang, X. Xu, Y. Liu, X. Yuan, Up-shifting the desalination rate limit of capacitive deionization via integrating chloride-capturing Bi nanocluster with flow-through cell architecture, Chem. Eng. J. 460 (2023) 141726.
[12] W. Xu, C. Tan, A. Wang, S. Hu, L. Deng, S. Boles, K. Sun, B. Li, H. Hu, Interlayer structure and chemistry engineering of MXene-based anode for effective capture of chloride anions in asymmetric capacitive deionization, ACS Appl. Mater. Interfaces 15 (2023) 16266–16276.
[13] X. Zhang, H. Zhou, Z. He, H. Zhang, H. Zhao, Flow-electrode capacitive deionization utilizing three-dimensional foam current collector for real seawater desalination, Water Res. 220 (2022) 118642.
[14] N. Kim, E.-a. Lee, X. Su, C. Kim, Parametric investigation of the desalination performance in multichannel membrane capacitive deionization (MC-MCDI), Desalination 503 (2021) 114950.
[15] A. Shrivastava, V.Q. Do, K.C. Smith, Efficient, selective sodium and Lithium removal by faradaic deionization using symmetric sodium titanium vanadium phosphate intercalation electrodes, ACS Appl. Mater. Interfaces 14 (2022) 30672–30682.
[16] T. Kim, C.A. Gorski, B.E. Logan, Low energy desalination using battery electrode deionization, Environ. Sci. Technol. Lett. 4 (2017) 444–449.
[17] L. Hackl, S.-W. Tsai, B. Kalyan, C.-H. Hou, A. Gadgil, Electrically regenerated ion-exchange technology: leveraging faradaic reactions and assessing the effect of co-ion sorption, J. Colloid Interface Sci. 623 (2022) 985–991.
[18] S. Porada, L. Zhang, J.E. Dykstra, Energy consumption in membrane capacitive deionization and comparison with reverse osmosis, Desalination 488 (2020) 114383.
[19] Q. Wu, D. Liang, S. Lu, J. Zhang, H. Wang, Y. Xiang, D. Aurbach, Novel inorganic integrated membrane electrodes for membrane capacitive deionization, ACS Appl. Mater. Interfaces 13 (2021) 46537–46548.
[20] O. Sufiani, J. Elisadiki, H. Tanaka, K. Teshima, M.G. Sahini, R.L. Machunda, Y.A. C. Jande, Adsorption-capacitive deionization hybrid system with activated carbon of modified potential of zero charge, Environ. Res. 219 (2023) 115114.
[21] B. Chen, A. Feng, R. Deng, K. Liu, Y. Yu, L. Song, MXene as a cation-selective cathode material for asymmetric capacitive deionization, ACS Appl. Mater. Interfaces 12 (2020) 13750–13758.
[22] K. Wang, Y. Liu, X. Xu, Y. Jiao, L. Pan, In situ synthesis of ultrasmall $NaTi_2(PO_4)_3$ nanocube decorated carbon nanofiber network enables ultrafast and superstable rocking-chair capacitive deionization, Chem. Eng. J. 463 (2023) 142394.
[23] K. Luo, Q. Niu, Y. Zhu, B. Song, G. Zeng, W. Tang, S. Ye, J. Zhang, M. Duan, W. Xing, Desalination behavior and performance of flow-electrode capacitive deionization under various operational modes, Chem. Eng. J. 389 (2020) 124051.
[24] E. Liu, L.Y. Lee, S.L. Ong, H.Y. Ng, Treatment of industrial brine using capacitive deionization (CDI) towards zero liquid discharge – challenges and optimization, Water Res. 183 (2020) 116059.
[25] M. Liu, Z. Xue, H. Zhang, Y. Li, Dual-channel membrane capacitive deionization based on asymmetric ion adsorption for continuous water desalination, Electrochem. Commun. 125 (2021) 106974.
[26] J. Lee, K. Jo, J. Lee, S.P. Hong, S. Kim, J. Yoon, Rocking-chair capacitive deionization for continuous brackish water desalination, ACS Sustain. Chem. Eng. 6 (2018) 10815–10822.
[27] G. Mohandass, W. Chen, S. Krishnan, T. Kim, Asymmetric and symmetric redox flow batteries for energy-efficient, high-recovery water desalination, Environ. Sci. Technol. 56 (2022) 4477–4488.
[28] Z. Tan, W. Wang, M. Zhu, Y. Liu, Y. Yang, X. Ji, Z. He, $Ti_3C_2T_x$ MXene@carbon dots hybrid microflowers as a binder-free electrode material toward high capacity capacitive deionization, Desalination 548 (2023) 116267.
[29] D.D. Le Pevelen, Small molecule X-ray crystallography, theory and workflow, in: J. C. Lindon (Ed.), Encyclopedia of Spectroscopy and Spectrometry (Second Edition), Academic Press, Oxford, 2010, pp. 2559–2576.
[30] V. Augustyn, P. Simon, B. Dunn, Pseudocapacitive oxide materials for high-rate electrochemical energy storage, Energ. Environ. Sci. 7 (2014) 1597–1614.
[31] J. Du, W. Xing, J. Yu, J. Feng, L. Tang, W. Tang, Synergistic effect of intercalation and EDLC electrosorption of 2D/3D interconnected architectures to boost capacitive deionization for water desalination via $MoSe_2$/mesoporous carbon hollow spheres, Water Res. 235 (2023) 119831.
[32] J. Yan, W. Xiao, L. Chen, Z. Wu, J. Gao, H. Xue, Superhydrophilic carbon nanofiber membrane with a hierarchically macro/meso porous structure for high performance solar steam generators, Desalination 516 (2021) 115224.
[33] H. Wang, W. Wang, H. Wang, Y. Li, X. Jin, H. Niu, H. Wang, H. Zhou, T. Lin, Improving supercapacitance of electrospun carbon nanofibers through increasing micropores and microporous surface area, Adv. Mater. Interfaces 6 (2019) 1801900.
[34] K. Sun, X. Yao, B. Yang, F. Jia, S. Song, Oxygen-incorporated molybdenum disulfide nanosheets as electrode for enhanced capacitive deionization, Desalination 496 (2020) 114758.
[35] Y. Liu, X. Du, Z. Wang, L. Zhang, Q. Chen, L. Wang, Z. Liu, X. Dou, H. Zhu, X. Yuan, MoS_2 nanoflakes-coated electrospun carbon nanofibers for "rocking-chair" capacitive deionization, Desalination 520 (2021) 115376.
[36] W. Peng, W. Wang, G. Han, Y. Huang, Y. Zhang, Fabrication of 3D flower-like MoS_2/graphene composite as high-performance electrode for capacitive deionization, Desalination 473 (2020) 114191.
[37] A. Manivel, G.-J. Lee, C.-Y. Chen, J.-H. Chen, S.-H. Ma, T.-L. Horng, J.J. Wu, Synthesis of MoO_3 nanoparticles for azo dye degradation by catalytic ozonation, Mater. Res. Bull. 62 (2015) 184–191.
[38] Y. Cai, W. Zhang, R. Fang, D. Zhao, Y. Wang, J. Wang, Well-dispersed few-layered MoS_2 connected with robust 3D conductive architecture for rapid capacitive deionization process and its specific ion selectivity, Desalination 520 (2021) 115325.
[39] X. Zheng, J. Xu, K. Yan, H. Wang, Z. Wang, S. Yang, Space-confined growth of MoS_2 nanosheets within graphite: the layered hybrid of MoS_2 and graphene as an active catalyst for hydrogen evolution reaction, Chem. Mater. 26 (2014) 2344–2353.
[40] Y. Deng, L.R.L. Ting, P.H.L. Neo, Y.-J. Zhang, A.A. Peterson, B.S. Yeo, Operando Raman spectroscopy of amorphous molybdenum sulfide (MoS_x) during the electrochemical hydrogen evolution reaction: identification of sulfur atoms as catalytically active sites for H^+ reduction, ACS Catal. 6 (2016) 7790–7798.
[41] Y. Duan, H. Fu, L. Zhang, R. Gao, Q. Sun, Z. Chen, H. Du, Embedding of ultra-dispersed MoS_2 nanosheets in N,O heteroatom-modified carbon nanofibers for improved adsorption of Hg^{2+}, Composites Communications 31 (2022) 101106.
[42] S. Ghosh, W.D. Yong, E.M. Jin, S.R. Polaki, S.M. Jeong, H. Jun, Mesoporous carbon nanofiber engineered for improved supercapacitor performance, Korean J. Chem. Eng. 36 (2019) 312–320.
[43] B.K. Tarus, Y.A.C. Jande, K.N. Njau, Electrospun carbon nanofibers for use in the capacitive desalination of water, New Carbon Mater. 37 (2022) 1066–1084.
[44] T. Yin, Y. Zhang, D. Dong, T. Wang, J. Wang, Highly efficient capacitive removal of Cd^{2+} over MoS_2-carbon framework composite material in desulphurisation wastewater from coal-fired power plants, J. Clean. Prod. 355 (2022) 131814.
[45] G. Jia, D. Chao, N.H. Tiep, Z. Zhang, H.J. Fan, Intercalation Na-ion storage in two-dimensional $MoS_{2-x}Se_x$ and capacity enhancement by selenium substitution, Energy Storage Materials 14 (2018) 136–142.
[46] F. Maroni, S. Dongmo, C. Gauckler, M. Marinaro, M. Wohlfahrt-Mehrens, Through the maze of multivalent-ion batteries: a critical review on the status of the research on cathode materials for Mg^{2+} and Ca^{2+} ions insertion, Batteries Supercaps 4 (2021) 1221–1251.
[47] Z. Liu, X. Shang, H. Li, Y. Liu, A brief review on high-performance capacitive deionization enabled by intercalation electrodes, Global Chall. 5 (2021) 2000054.
[48] T. Ying, Y. Xiong, H. Peng, R. Yang, L. Mei, Z. Zhang, W. Zheng, R. Yan, Y. Zhang, H. Hu, C. Ma, Y. Chen, X. Xu, J. Yang, D. Voiry, C.Y. Tang, J. Fan, Z. Zeng, Achieving exceptional volumetric desalination capacity using compact MoS_2 nanolaminates, Advanced Materials, n/a 2403385 (2024).
[49] L. Wang, M. Torkamanzadeh, A. Majed, Y. Zhang, Q. Wang, B. Breitung, G. Feng, M. Naguib, V. Presser, Time-dependent cation selectivity of titanium carbide MXene in aqueous solution, Advanced Sustainable Systems 6 (2022) 2100383.
[50] Q. Gao, W. Sun, P. Ilani-Kashkouli, A. Tselev, P.R.C. Kent, N. Kabengi, M. Naguib, M. Alhabeb, W.-Y. Tsai, A.P. Baddorf, J. Huang, S. Jesse, Y. Gogotsi, N. Balke, Tracking ion intercalation into layered Ti_3C_2 MXene films across length scales, Energ. Environ. Sci. 13 (2020) 2549–2558.
[51] Z. Chen, X. Xu, Y. Liu, J. Li, K. Wang, Z. Ding, F. Meng, T. Lu, L. Pan, Ultra-durable and highly-efficient hybrid capacitive deionization by MXene confined MoS_2 heterostructure, Desalination 528 (2022) 115616.
[52] P. Srimuk, J. Lee, S. Fleischmann, S. Choudhury, N. Jäckel, M. Zeiger, C. Kim, M. Aslan, V. Presser, Faradaic deionization of brackish and sea water via pseudocapacitive cation and anion intercalation into few-layered molybdenum disulfide, J. Mater. Chem. A 5 (2017) 15640–15649.
[53] V. Pothanamkandathil, J. Fortunato, C.A. Gorski, Electrochemical desalination using intercalating electrode materials: a comparison of energy demands, Environ. Sci. Technol. 54 (2020) 3653–3662.
[54] H. Zhu, X. Qin, L. Cheng, A. Azcatl, J. Kim, R.M. Wallace, Remote plasma oxidation and atomic layer etching of MoS_2, ACS Appl. Mater. Interfaces 8 (2016) 19119–19126.
[55] W. Shi, X. Liu, C. Ye, X. Cao, C. Gao, J. Shen, Efficient lithium extraction by membrane capacitive deionization incorporated with monovalent selective cation exchange membrane, Sep. Purif. Technol. 210 (2019) 885–890.
[56] H. Yu, S.M. Hossain, C. Wang, Y. Choo, G. Naidu, D.S. Han, H.K. Shon, Selective lithium extraction from diluted binary solutions using metal-organic frameworks (MOF)-based membrane capacitive deionization (MCDI), Desalination 556 (2023) 116569.
[57] A. Battistel, M.S. Palagonia, D. Brogioli, F. La Mantia, R. Trócoli, Electrochemical methods for Lithium recovery: a comprehensive and critical review, Adv. Mater. 32 (2020) 1905440.